



# *In vitro* bioactivity and antibacterial performances of atmospheric plasma sprayed *c*-axis preferential oriented hydroxyapatite coatings

Xiaomei Liu<sup>a</sup>, Dingyong He<sup>a,c,\*</sup>, Zheng Zhou<sup>a,c</sup>, Xingye Guo<sup>a,c</sup>, Yi Liu<sup>b,d</sup>, Wenjia Hou<sup>b,d</sup>, Hua Li<sup>b,d,\*\*</sup>

<sup>a</sup> Faculty of Materials and Manufacturing, Beijing University of Technology, Beijing 100124, China

<sup>b</sup> Key Laboratory of Marine Materials and Related Technologies, Zhejiang Key Laboratory of Marine Materials and Protective Technologies, Ningbo Institute of Materials Technology and Engineering, Chinese Academy of Sciences, Ningbo 315201, China

<sup>c</sup> Beijing Engineering Research Center of Eco-Materials and LCA, Beijing 100124, China

<sup>d</sup> Zhejiang Engineering Research Center for Biomedical Materials, Cixi Institute of Biomedical Engineering, Ningbo Institute of Materials Technology and Engineering, Chinese Academy of Sciences, Ningbo 315201, China

## ARTICLE INFO

### Keywords:

Hydroxyapatite  
Atmospheric plasma spraying  
Crystalline orientation  
Bioactivity  
Antibacterial activity

## ABSTRACT

Atmospheric plasma spraying (APS) is widely used in the fabrication of hydroxyapatite (HA) coating due to the advantages of low-cost, simple operation and it can be used to fabricate coatings with controllable structure. Despite all these advantages, the application of APS deposited HA coating for long-term use is limited by its low crystallinity, low phase purity and poor antibacterial property efficiency. Herein, HA coatings with high crystallinity, phase purity and *c*-axis crystalline orientation were fabricated by APS. *In vitro* cell, culture testing suggested that the *c*-axis oriented HA coating was more effective to promote the proliferation of osteoblasts cells compared with other coatings. The antibacterial activity of HA coating against the bacteria indicated that the *c*-axis oriented HA coating restrained the bacterial adhesion, and the antibacterial effect of the *E. coli* bacteria was more pronounced than that of the *S. epidermidis* bacteria. This study suggests that the HA coatings with the specific *c*-axis crystalline orientation are available for their potential applications for orthopedic and dental implantation.

## 1. Introduction

Titanium and its alloys are widely used in dentistry and orthopaedics for many years owing to their excellent mechanical properties and biocompatibility [1]. However, their poor osseointegration keeps as a big concern limiting their long-term use as biomedical implants [2]. Therefore, the surface modification of titanium-based alloys is essential to improve their osseointegration for successful biomedical applications.

Hydroxyapatite (HA), the main mineral component of bone and teeth, has been successfully used in various biomedical applications such as dentistry, orthopedic, and drug delivery system [3,4]. However, the mechanical strength of HA is insufficient for load-bearing applications due to its strength limitation. To enhance bone integration of implants and improve their lifetime, the HA coatings can be deposited on the

surface of implanted metallic parts which promote the early establishment of bone-implant integration and protect the body from the harmful metallic ions of the implanted metallic parts [3,5].

HA can be deposited on metallic implants through a variety of techniques, such as sol-gel [6], physical vapour deposition (PVD) [7], chemical vapour deposition (CVD) [8], thermal spraying technique [9–11], and other techniques [12,13]. Due to the low cost, easy operation, controllable microstructure and good mechanical properties of the deposited coatings, plasma spraying technique is successfully applied for HA coating deposition [4,14]. Among various plasma spraying techniques, atmospheric plasma spraying (APS) is the most widely used technique to fabricate HA coatings. However, the plasma-sprayed HA coatings often contain undesired phases, *i.e.*,  $\alpha$ -tri-calcium phosphate ( $\alpha$ -TCP),  $\beta$ -tri-calcium phosphate ( $\beta$ -TCP), tetra-calcium phosphate

\* Corresponding authors at: Beijing University of Technology, 100 Ping Le Yuan, Chaoyang District, Beijing 100124, China.

\*\* Corresponding authors at: Ningbo Institute of Materials Technology and Engineering, Chinese Academy of Sciences, No. 1219 Zhongguan West Road, Zhenhai District, Ningbo City, Zhejiang Province 315201, China.

E-mail addresses: [liuxiaomei@emails.bjut.edu.cn](mailto:liuxiaomei@emails.bjut.edu.cn) (X. Liu), [dyhe@bjut.edu.cn](mailto:dyhe@bjut.edu.cn) (D. He), [zhouzhengbjut@bjut.edu.cn](mailto:zhouzhengbjut@bjut.edu.cn) (Z. Zhou), [xyguo@bjut.edu.cn](mailto:xyguo@bjut.edu.cn) (X. Guo), [liuyi@nimte.ac.cn](mailto:liuyi@nimte.ac.cn) (Y. Liu), [houwenjia@nimte.ac.cn](mailto:houwenjia@nimte.ac.cn) (W. Hou), [lihua@nimte.ac.cn](mailto:lihua@nimte.ac.cn) (H. Li).

<https://doi.org/10.1016/j.surfcoat.2021.127209>

Received 24 January 2021; Received in revised form 15 April 2021; Accepted 16 April 2021

Available online 23 April 2021

0257-8972/© 2021 Elsevier B.V. All rights reserved.

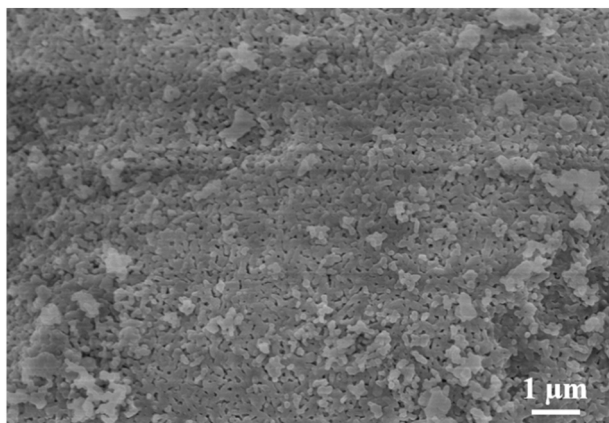


Fig. 1. Surface micrograph of HA starting powder.

(TTCP), or even calcium oxide (CaO) [4,10]. Moreover, the amorphous calcium phosphate (ACP) phase is usually found in the plasma-sprayed HA coating due to the rapid quenching of molten particles on metal substrate during the deposition process and because of selective evaporation of some oxides [15]. The dissolution behavior of HA coating in body fluid is influenced by its phase structure. For example, decomposition phases and ACP show a higher dissolution rate in body fluid than crystalline HA, which accelerates the failure of the coated implants [16]. Excessive levels of dissolution can also lead to a significant rise of local pH values, giving rise to cytotoxic effects on bone cells [17,18]. In addition, the HA coating with high crystallinity and high purity is desired for long-term implantation and safety application. Similarly, the dissolution behavior of HA coating is also influenced by its crystallographic texture. Previously, we found that the HA coating with (002) crystallographic texture deposited by micro-plasma spraying showed higher chemical stability in Hanks' solution than the HA coating with the random orientation [19]. Therefore, we attempted to fabricate HA coatings with well-crystallized HA and (002) crystal texture using the APS technique in our previous research and successfully fabricated by adjusting the APS spraying parameters [20]. However, the influence of (002) crystal texture on the adhesion and differentiation of osteoblasts is rarely studied. Hence, the influence of (002) crystalline orientation on the attachment and proliferation of osteoblasts is further investigated in this research.

Apart from biocompatibility, the bacterial infection is another serious problem in bone surgery operation and is the main cause of implant failure. In the body environment, bacterial biofilm tends to easily generate on the artificial implant surface, leading to implant failure and bone destruction, or even systemic toxicity [21]. Regardless of their excellent biocompatibility and osteoconductivity, the conventional plasma-sprayed HA coatings deposited on the titanium alloy substrate still bear the problem of bacterial infection [22,23]. Therefore, considering the influence of surface characteristic (such as, topography, surface roughness, hydrophilicity) of implant on the attachment of bacteria, the antibacterial activities are evaluated by measuring the adhesion of Gram-negative bacteria and Gram-positive bacteria to the coating surface.

## 2. Materials and methods

### 2.1. Coating preparation

Commercial spherical agglomerated HA powders with the particle size of 38–45 μm (Medicoat AG, Mägenwil, Switzerland) were used for the fabrication of HA coatings. Fig. 1 shows the morphology of HA powder at high magnification, suggesting that the HA powders were formed of nano HA particles (70–200 nm). Ti6Al4V disks (Φ15 mm x 3

Table 1

APS parameters for deposition of HA coatings.

	A1	A2	A3
Current (A)	350	350	350
Voltage (V)	50	50	50
Flow rate of argon (NL/min)	40	23	23
Spraying distance (mm)	55	55	110

Table 2

The liquid surface energy (mN/m).

Liquid	$\gamma_{LV}^d$	$\gamma_{LV}^p$	$\gamma_{LV}$
Deionized water	21.8	51.0	72.8
Glycerin	34.0	30.0	64

mm) were used as the substrates. Prior to the coating deposition, the substrates were grit-blasted and then ultrasonically cleaned in acetone. Atmospheric plasma spraying system (APS, Sulzer Metco 9 M, Switzerland) equipped with 9 MB plasma spray gun and GH7 nozzle was used to deposit three kinds of HA coatings with different phase structures. These APS parameters were selected according to the previously

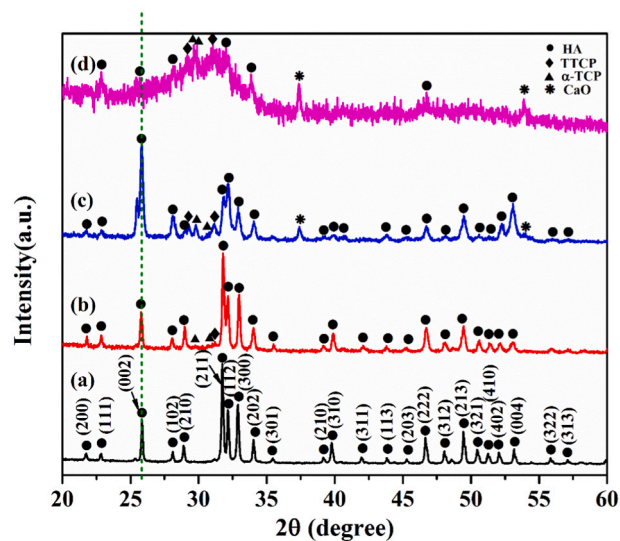


Fig. 2. XRD spectra of the starting powder and the as-sprayed coatings: (a) HA starting powder, (b) coating A1, (c) coating A2, (d) coating A3.

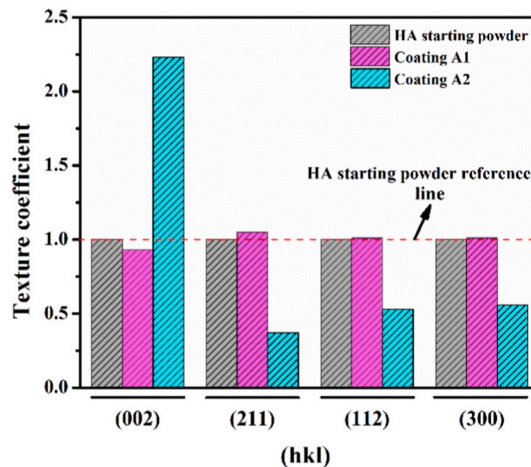
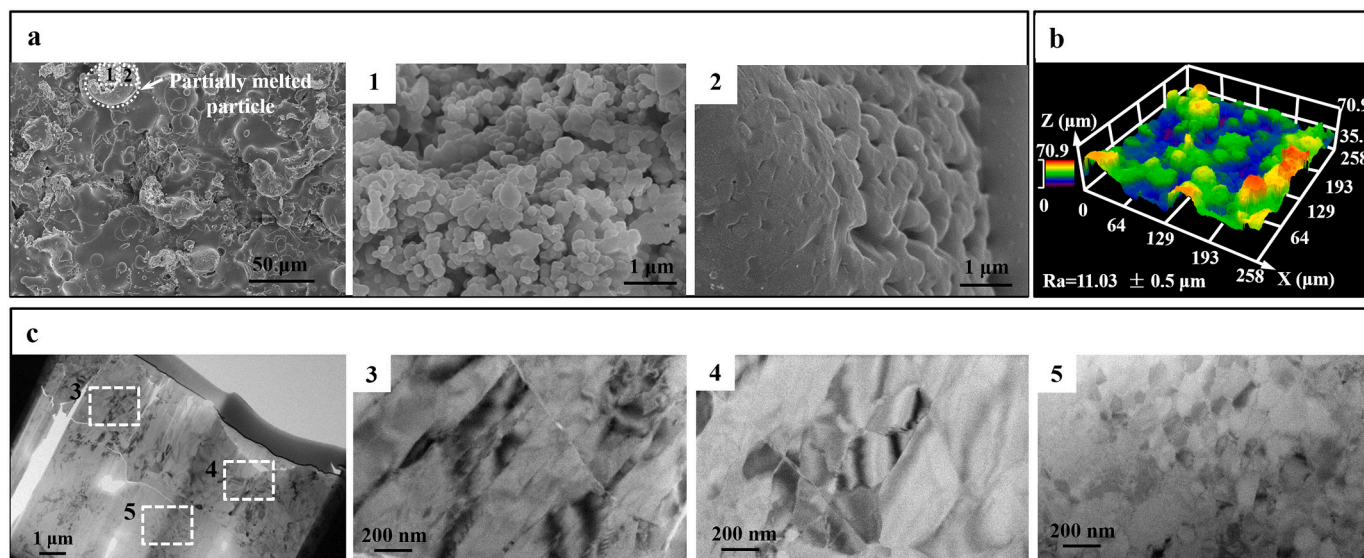


Fig. 3. Texture coefficients of the HA starting powder, coating A1 and coating A2.



**Fig. 4.** Morphologies of the surface and cross-section of coating A1: (a) SEM images of the coating surface, picture 1 shows the high magnification morphology of area 1, picture 2 shows the high magnification morphology of area 2; (b) three-dimensional image of the coating surface and (c) cross-sectional TEM images, picture 3, 4, 5 show the high magnification morphology of the area 3, 4, 5 in the low magnification image respectively.

published study [20]. These three kinds of HA coatings were named A1, A2 and A3, respectively. Table 1 listed the APS spray parameters used in this study.

## 2.2. Coating characterization

The surface features, including surface morphology, surface roughness and surface energy, play major roles in the *in vitro* responses of HA coating. Herein, surface morphologies of the starting HA powder and coatings were characterized using a field emission scanning electron microscope (FE-SEM, FEI Quanta FEG250, USA). Surface roughness and

3D morphology of the coatings were studied by laser scanning confocal microscopy (LSCM, OLS4100, Japan). The cross-sectional morphologies of those three kinds of HA coatings were also observed using Transmission Electron Microscopy (TEM, JEM-2100F) to further examine the grain size of the HA coatings. The TEM samples were prepared using a focused ion beam (FIB, FEI Helios-600i, USA) dual-beam system method. The phase structure of the coating and the starting powder were measured using X-ray diffraction (XRD, D8 ADVANCE, Germany) with Cu K radiation at the operating conditions of 40 kV and 30 mA. The crystallinity of the coating was calculated using the Rutland Method [24]. The Texture Coefficient (TC) was also calculated in following

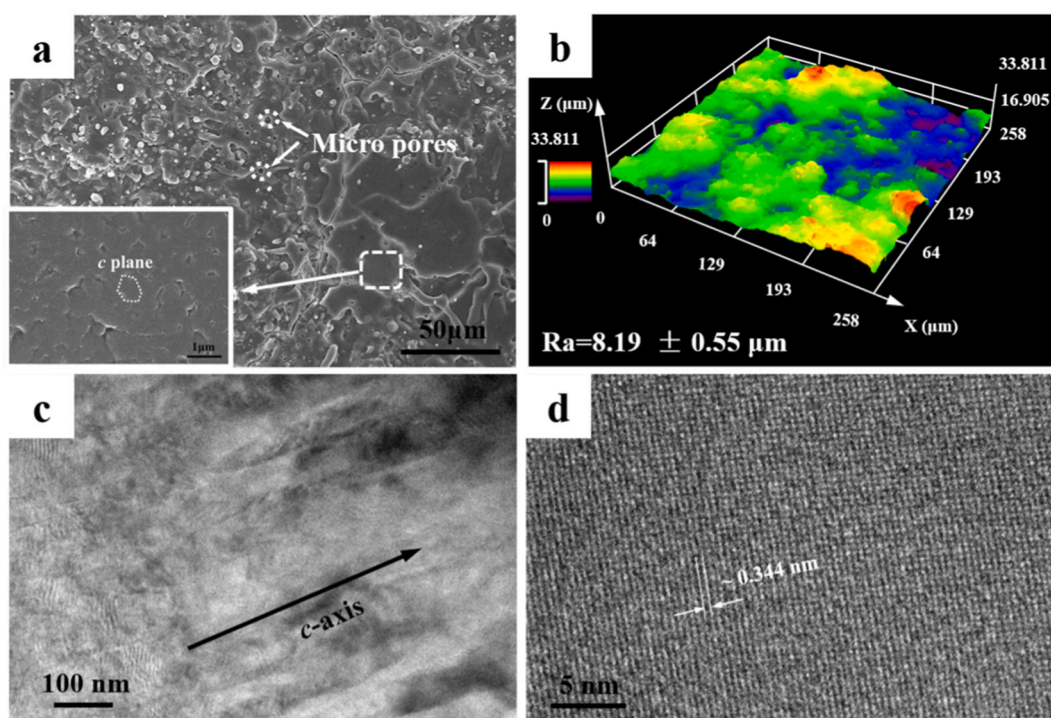


**Fig. 5.** Morphologies of the surface and cross-section of coating A2: (a) SEM images of the coating surface, (b) three-dimensional image of the coating surface, (c) cross-sectional TEM image and (d) high resolution TEM image.

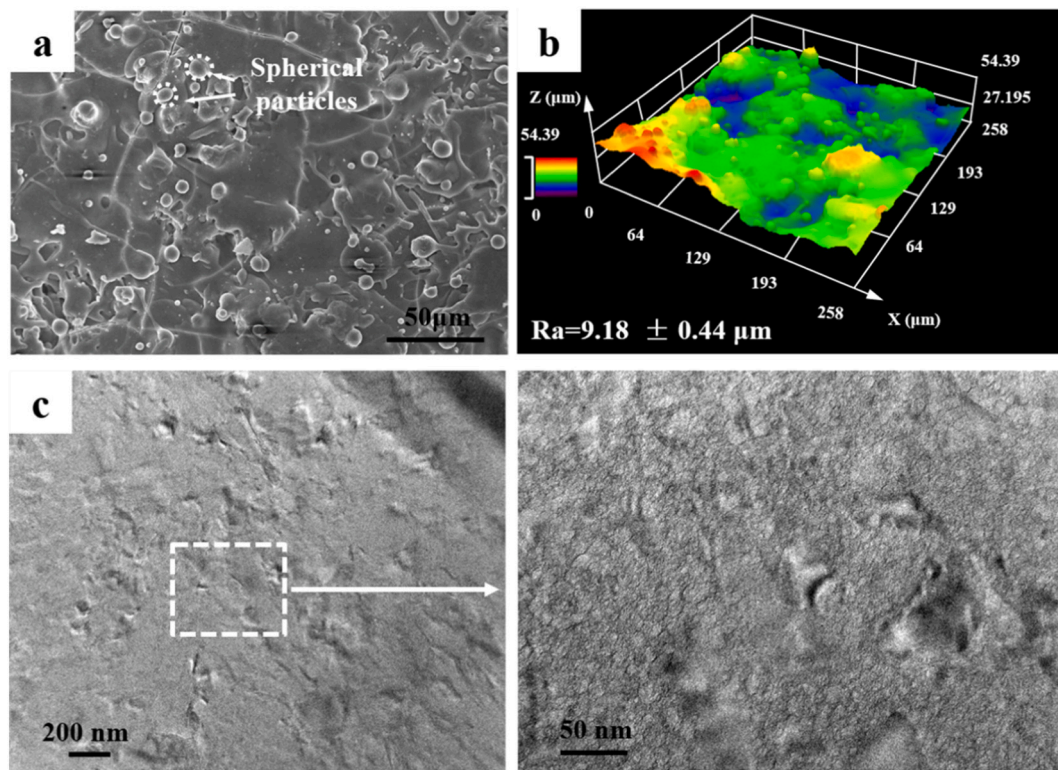


Fig. 6. Morphologies of the surface and cross-section of coating A3: (a) SEM images of the coating surface, (b) three-dimensional image of the coating surface and (c) cross-sectional TEM images.

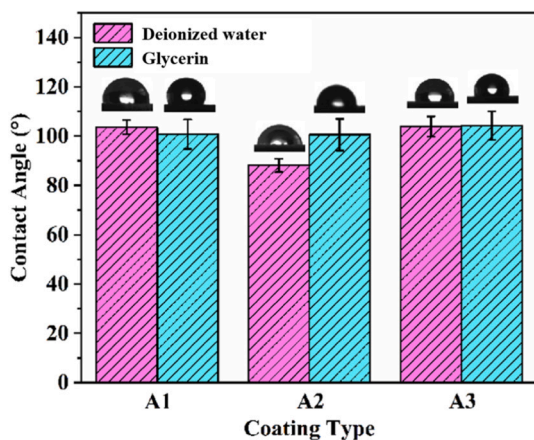


Fig. 7. Contact angles of deionized water and glycerin drops on the surface of coatings A1, A2, and A3.

formula [25,26]:

$$TC(hkl) = \frac{I_{o(hkl)} / I_{o(hkl)}}{\frac{1}{N} \sum_{(hkl)=1}^N (I_{(hkl)} / I_{o(hkl)})}$$

where  $I_{(hkl)}$  was the integral intensity of the  $(hkl)$  diffraction peaks for coating specimen.  $I_{o(hkl)}$  was the integral intensity for starting HA powder with the same  $(hkl)$  diffraction peaks. In this study, the (002) diffraction peak and the three strongest diffraction peaks of HA ((211), (112) and (300)) were selected, therefore  $N = 4$ .

To evaluate the surface energy of the coatings, contact angles of two different liquids (deionized water and glycerin) on coating surfaces were determined by measuring the tangent angle between the coating surface and the liquid using a contact angle optical system (OCA20, Germany)

[27,28]. For each case, at least five drops of each liquid were measured to get an average contact angle. The surface energy of the coating was calculated by using the following equation [29,30]:

$$\gamma_{LV}(1 + \cos\theta) = 2(\gamma_{SV}^p \gamma_{LV}^p)^{1/2} + 2(\gamma_{SV}^d \gamma_{LV}^d)^{1/2}$$

$$\gamma_{SV} = \gamma_{SV}^p + \gamma_{SV}^d$$

where  $\theta$  was the contact angle,  $\gamma_{LV}$  was the liquid-gas interfacial tension, and  $\gamma_{SV}$  was the solid-gas interfacial tension, respectively. The superscript p of the  $\gamma_{SV}$  and  $\gamma_{LV}$  represented the polar tension component of the interfacial free energy. The superscript d of the  $\gamma_{SV}$  and  $\gamma_{LV}$  represented the dispersion tension component of the interfacial free energy. The polar and dispersion surface tension components of the liquids of the deionized water and glycerin are shown in Table 2 [31].

### 2.3. In vitro bioactivity evaluation

#### 2.3.1. Biological testing

Attachment and proliferation of human osteoblast cells on the HA coatings were examined. The human osteoblast cells, HFOB 1.19 SV40 transfected osteoblasts were used. The  $\alpha$ -minimum essential medium ( $\alpha$ -MEM) (SH30265.01B, HyClone, USA) supplemented with 10% heat-inactivated fetal bovine serum, 100 U/mL penicillin and 100  $\mu$ g/mL streptomycin were used to cultivate the cells under an atmosphere of 100% humidity and 5% CO<sub>2</sub> at 37 °C [32]. Samples were sterilized at 121 °C for 15 min by the autoclave and pressure cooker. Subsequently, cells at the density of  $6 \times 10^4$  cells/cm<sup>2</sup> were seeded in 24-well cell culture plate containing the coating samples with 1 mL media in each well.

After culturing for 1 day, 5 days and 7 days, the cell viability was measured using methyl thiazole tetrazodium (MTT) (Sigma, St Louis, MO, USA) test according to a well-established protocol [32]. In order to observe the cells adhering to the coating surface by the SEM, the samples

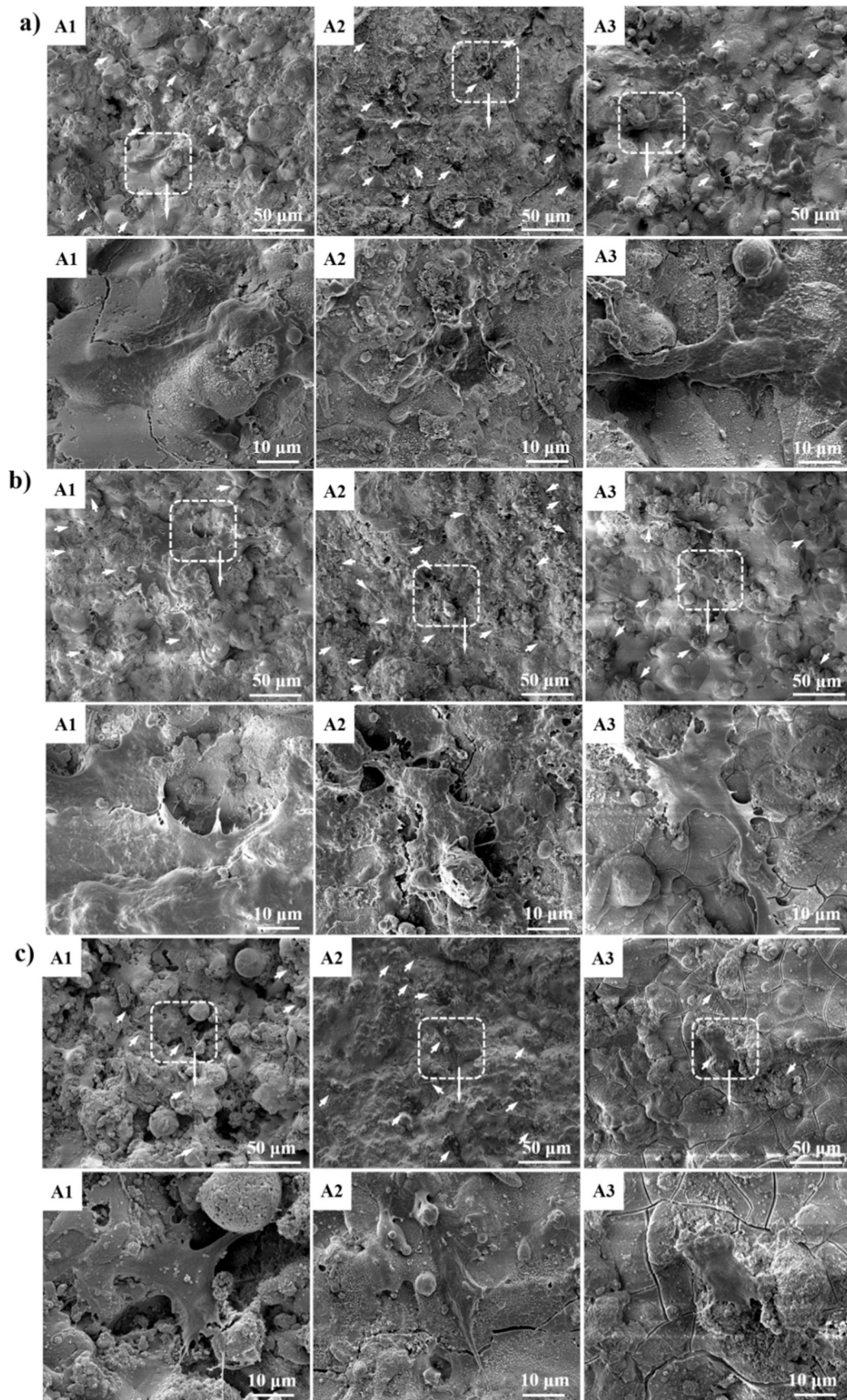


Fig. 8. Surface morphology of the coating A1, A2 and A3 after the incubation time of a) 1 day, b) 5 days and c) 7 days.

were washed twice with phosphate-buffered saline (PBS) solution to remove the non-adherent cells. Then, 1 mL of 2.5% paraformaldehyde was added to fix the adhered cells. After 2 h, the cells were washed twice with PBS solution and then dehydrated in graded ethanol solutions (25%, 50%, 75%, 90%, and 100%) for critical point drying. Before SEM observation, the thin platinum film was deposited on all samples.

### 2.3.2. Antibacterial testing

Gram-negative bacteria (*Escherichia coli* (*E. coli*, ATCC25922)) and Gram-positive bacteria (*Staphylococcus epidermidis* (*S. epidermidis*, ATCC12228)) were used in this study to evaluate the antibacterial performance of the coatings. *E. coli* was cultured in Luria-Bertani (LB) broth. *S. epidermidis* was cultured in Trypticase soy broth (TSB). After inoculation of a single bacteria colony, the media were shaken in a super-centrifuge (TG16-WS, Shanghai Lu Xiangyi Centrifuge Instrument Co., Ltd., China) at the rotate speed of 120 rpm for 24 h at 37 °C. The bacteria-containing culture medium was centrifuged at 2000 rpm for 5 min. After removal of the supernatant, the bacteria were washed with PBS and were resuspended in PBS at a concentration of  $10^8$  CFU/mL [33]. Sterilized samples were put into a 24-well plate and then 1 mL of the bacterial suspension was added to each well. Subsequently, the plate was incubated at 37 °C for 24 h. To observe the bacteria attachment behavior by SEM, the samples were washed twice with PBS to remove the non-adherent bacteria and fixed in the glutaraldehyde at 4 °C for 2 h and then were washed twice with PBS. Finally, these samples were dehydrated [34].

### 2.3.3. Chemical stability in phosphate-buffered saline

The HA coatings with different phase structures were immersed in PBS solution for assessing their chemical stability. Each coating sample was soaked in 1 mL PBS solution at 37 °C for 1 day, 5 days and 7 days. After immersion, the coating samples were washed with deionized water and dried at 37 °C. SEM characterization was conducted to investigate the surface morphology of the coatings after the immersion testing.

## 3. Results and discussion

Three kinds of HA coatings with different phase structures were successfully fabricated using different spraying parameters. The coating A1 exhibited high crystallinity (>90%) (Fig. 2b) and its phase composition was similar to that of the starting HA powder (Fig. 2a). This was because the short spray distance and high argon flow rate were insufficient to fully melt the in-flight particles. The microstructure of the A2 coatings had the (002) crystalline orientation characteristics and high crystallinity (> 85%), and also showed higher intensity of (002) peak than that of the starting HA powder and coating A1 (Fig. 2a–c). The texture coefficient of the HA powder, coating A1 and coating A2 were plotted in Fig. 3. It is clear that the TC(002) of coating A2 is higher than that of the HA starting powder and coating A1, which means that the coating A2 shows *c*-axis texture. The longer spray distance of 110 mm for the coating A3 triggered more severe decomposition of HA to TTCP,  $\beta$ -TCP or CaO and showed low crystallinity (<50%) (Fig. 2d). Meanwhile, much more ACP was formed in this coating due to the rapid quenching of the molten particles after impacting to a cold substrate. XRD patterns of coating A1 and coating A3 did not show (002) crystalline orientation. We have reported the preparation of those three kinds of HA coatings in our previous works where more detailed description about the structure formation mechanism of those coatings can be found [20].

Microstructure characterization showed that the coating A1 contained well-flattened splats and spherical particles in a partially melted state (Fig. 4a). The LSCM analysis revealed that the coating A1 with spherical particles showed an average roughness ( $R_a$ ) of  $11.03 \pm 0.50$   $\mu\text{m}$  (Fig. 4b). The further magnified view of the partially melted particle showed nanosized particles in the unmelted core (area 1, Fig. 4a), and these nanosized particles were like those observed in the HA starting

powder (Fig. 1). Based on Fig. 4a, the nanoscaled rods were seen in area 2 of the skin layer. The typical cross-sectional morphology of the coating A1 is shown in the Fig. 4c, it is observed that the coating microstructure is inhomogeneous. Columnar grains were observed in area 3 (Fig. 4c), which were about 50–200 nm in width and 2  $\mu\text{m}$  in height. The magnified morphology showed that large grains (150–400 nm) were distributed in area 4. As is shown in area 5, small grains in the range of 50–150 nm were observed. The short dwell time of the HA powders in the plasma jet during the plasma spraying helped to preserve the nanostructure of the agglomerated HA powders. Meanwhile, the rapid cooling of the coating A1 led to the formation of nanoscale grains with small size in these final coatings. The nanoparticles in the skin layer of the HA powder were grown into columnar grains under the plasma jet heating.

The coating A2 mainly consisted of well-flattened splats, and the splat was also revealed by SEM (Fig. 5a). As a result, the coating A2 showed a smoother surface than the coating A1 and its surface roughness was  $8.19 \pm 0.55$   $\mu\text{m}$  (Fig. 5b). Meanwhile, a few microsized pores with a size of 0.3–4.0  $\mu\text{m}$  were observed. The presence of the micropores in the top layer of the coating may promote cell in-growth and facilitate osteoblast growth [35]. The magnified surface microstructure revealed that there were columnar crystals in the coating A2 and the *c* plane of those columnar crystals was exposed on the surface of the coating A2 (Fig. 5a). The bright-field cross-sectional TEM image of coating A2 exhibited a columnar grain structure (Fig. 5c). The corresponding high-resolution TEM image is shown in Fig. 5d. The lattice spacing of  $\sim 0.344$  nm was observed in this image, which agreed well with the interplanar distance of *c* plane for hexagonal HA crystal.

The coating A3 showed well-flattened splats with splashing and small spherical particles (Fig. 6a). The presence of small spherical particles increased the surface roughness of coating A3 ( $9.18 \pm 0.44$   $\mu\text{m}$ ) as compared to that of the coating A2 (Fig. 6b). Fig. 6c exhibits a typical TEM structure of coating A3, where fine HA nanocrystals were distributed through an amorphous matrix. Due to the rapid cooling rate of the coating A3, the amorphous phase fraction was greatly increased, which was consistent with the XRD results (Fig. 2d).

The surface energy of an implant is known to affect its biological response such as biocompatibility and osteogenic ability. In this study, surface energy was calculated from contact angle measurements. The typical shape of deionized water and glycerin drops on each of the three types of surfaces are demonstrated in Fig. 7. The coating A1 with high surface roughness showed a water contact angle of  $103.6 \pm 2.9^\circ$ . For coating A2, the water contact angle was  $88.1 \pm 2.7^\circ$ . The water drops on the surface of coating A3 showed a contact angle of  $103.9 \pm 2.7^\circ$ . The surface energy calculated results showed that the coating A2 had a higher surface energy ( $20.59$   $\text{mJ}/\text{m}^2$ ) than the coating A1 ( $10.78$   $\text{mJ}/\text{m}^2$ ) and the coating A3 ( $10.83$   $\text{mJ}/\text{m}^2$ ). Previous studies suggested that

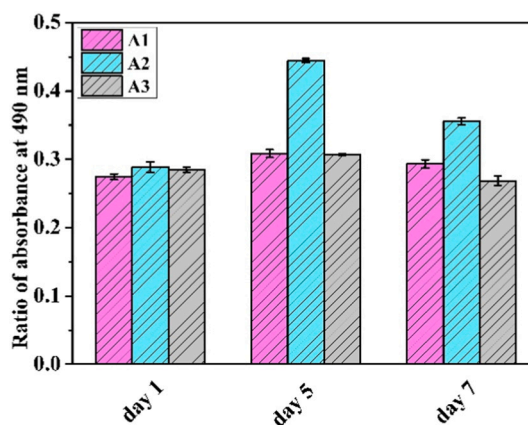


Fig. 9. Cell viability of the osteoblasts cultured on the surfaces of the coatings A1, A2 and A3.

the implant surface with higher surface energy triggered a more rapid cell activation [27,36]; therefore, the coating A2 deposited on metallic implants was likely to result in better biological performances than the other two coatings.

Cell responses such as cell proliferation, cell attachment and adhesion to an implanted biomaterial are essential for successful implantation. In this study, cell attachment and proliferation were investigated by SEM observation and MTT assay. Representative SEM micrographs illustrating cell morphology on all the coatings after 1 day, 5 days and 7 days of culture are shown in Fig. 8. Morphological analysis by SEM indicated that the cells were attached to all the coating samples. These SEM images demonstrated a higher number of cells attached on the surface of coating A2 than on the other coatings after 1-day culture

(Fig. 8a). As shown in Fig. 9, the MTT assessment suggested the highest percentage of cells attached and proliferated on the coating A2 after 1-day culture. The coating A2 accompanied by *c*-axis crystalline orientation facilitated the attachment of cells during the early culturing stage. High magnification morphological views of individual cells revealed that after 1-day incubation, the cells attached to the surface of coating A2 were a polygon with the lowest degree of cell spreading (Fig. 8a), and the smooth surface was likely to affect the spreading of the attached cells on the coating A2 surface. After 5 days of culturing, the number of cells growing on the coating A2 significantly increased, however, those on the other coatings showed minor changes. This was consistent with MTT assay results that showed an increase in attached cells on the coating A2 and no statistically significant difference on the other coatings (Fig. 9).

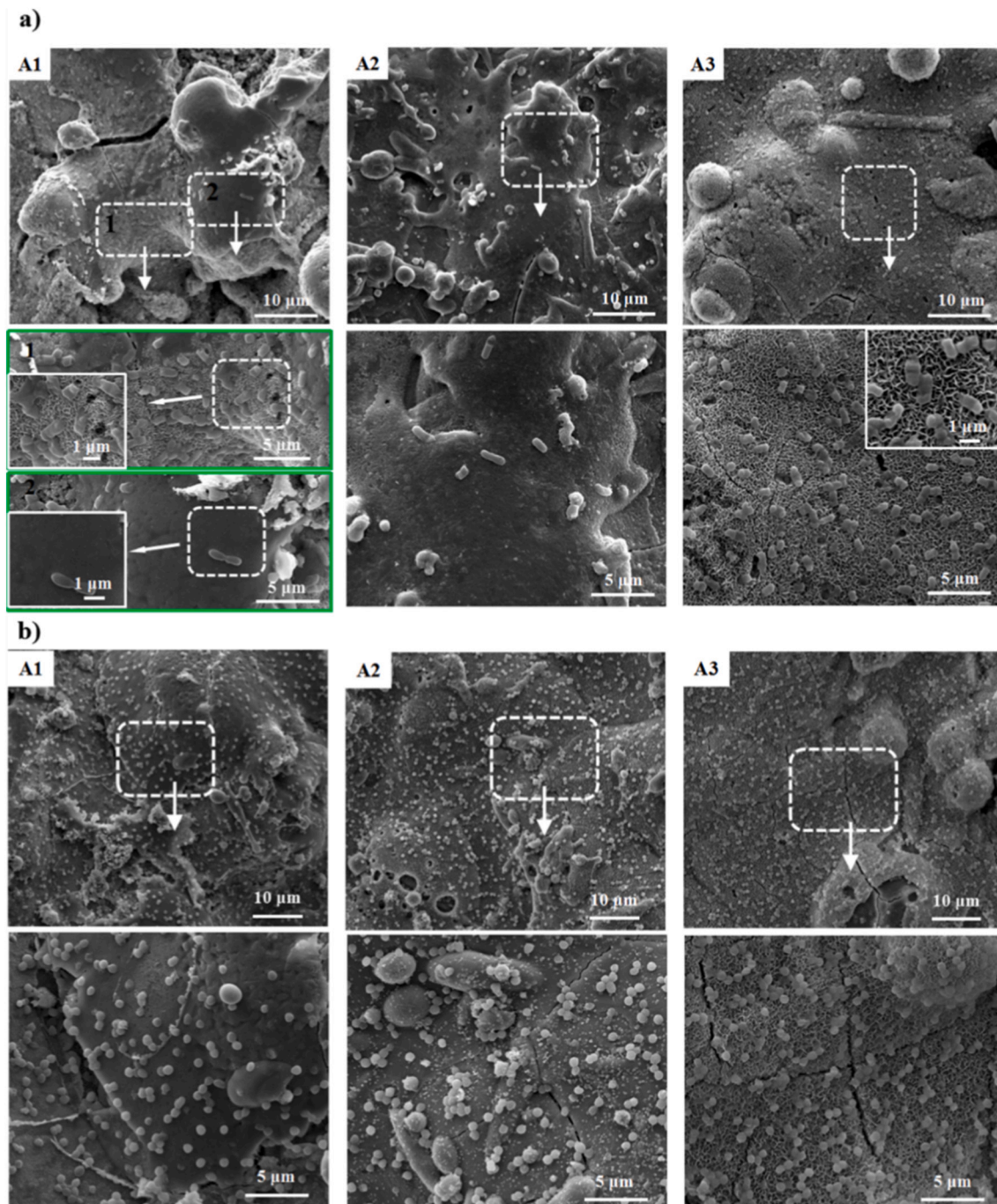


Fig. 10. Typical SEM photographs taken from the surfaces of the coatings after incubation in bacteria-containing media for 24 h: (a) *E. coli* and (b) *S. epidermidis*.

On both coating A1 and coating A2, fully spread cells with extended pseudopodia were clearly observed. The lowest spreading degree of the cells was seen on the surface of coating A3. After 7 days of incubation, the number of cells attached to all the coatings decreased and the spreading of the cells also shrunk. Whereas the morphology observation and the MTT assay results showed that the coating A2 favored the attachment and proliferation of the cells, and the proliferation ability of human osteoblast cells on the coating A2 were higher than those on the other coatings.

Cellular responses such as adhesion, spreading, proliferation and differentiation depend on the surface properties of implants [10,36]. Previous research results indicated that the material with higher surface energy enhances cell responses [36,37]. The phase composition of the HA coating usually plays an important role in regulating cell adhesion, spreading, and proliferation [38,39]. The well-crystallized HA coating benefits the adhesion and proliferation of cells as compared to the poorly crystallized HA coatings. However, cell spreading on the surface of amorphous HA coatings is greater than that on the well-crystallized HA coating. In addition, the influence of surface roughness on the cellular response has also been reported [40]. The proliferation of MG63 cells decreased with the increase of surface roughness. In this study, the high surface energy, high crystallinity and low surface roughness of the coating A2 with a *c*-axis crystalline orientation provided more favourable conditions for osteoblasts proliferation. In addition, the coating A2 showed the *c* plane exposed on its surface (Fig. 4c), whereas the *c* plane of hexagonal HA was rich in phosphate and hydroxide ions and was a negatively charged crystal plane [41]. The cell proliferation was promoted on the negatively charged surface [42,43]. While the cell viability decreased on all the coatings with the increasing of incubation time to 7 days (Fig. 9), which might be attributed to the dissolution of HA coating and the precipitation of apatite.

The implant-associated infection was initiated in the bacterial adhesion to the implant surface, and the fabrication of an anti-adhesive surface was one of the two primary categories for the prevention or limitation of implant-associated infection [44]. Therefore, the adhesion of bacteria on these three kinds of coatings was investigated by using the Gram-negative bacteria (*E. coli*) and Gram-positive bacteria (*S. epidermidis*). Bacterial adhesion on all coatings was shown in the Fig. 10. The density of adhered bacteria on all coatings was summarized in Fig. 11. These results showed that after 24 h culture the number of *E. coli* adhered on the surface of the coating A2 was much less than that on the surface of other coatings (Figs. 10a and 11). However, the reduction in the number of *S. epidermidis* adhered on the surface of coating A2 was not obvious as *E. coli* (Figs. 10b and 11). These results suggested that the *c*-axis oriented HA coating had high antibacterial activities against the Gram-negative bacteria, and the antibacterial activities against the Gram-positive bacteria were not prominent as the Gram-negative bacteria.

The surface features, such as surface topography, surface roughness, surface hydrophobicity/hydrophilicity and surface charge, play an important role in the bacterial adhesion [45,46]. From the observation of three-dimensional images, more bumps or peaks were observed on the surface of coating A1 and A3 compared with coating A2. These bumps can be the favourable anchor spot for the bacteria [45]. More notably, after 24 h immersion in bacterial suspensions, the surface morphology of all coatings changed. More pores were observed on coating A1 and coating A3, and many bacteria attached to the area with porous structure (Fig. 10a, A1, area 2 and a, A3). However, for the smooth area (Fig. 10a, A1, area1 and a, A2), a small number of bacteria were observed. Fig. 11 shows the surface morphologies of all the coatings after immersion in bacteria-free PBS solution for 1 day, 5 days and 7 days. As shown in Fig. 11a, plate-like crystals appeared on the surface of the coating A1 and coating A3 after 1-day immersion in bacteria-free PBS solution. This morphological feature of crystalline HA was consistent with previous findings that shown the formation of plate-like HA crystals on the Ti plate after the bioactivity testing in PBS [47]. On the

contrary, no plate-like crystals were observed on the surface of coating A2 after immersion for 1 day (Fig. 12a). Surface of the coating A1 and A3 after immersion for 5 days showed that the growth of plate-like crystals was enhanced and an apatite layer was formed (Fig. 12b). A small amount of apatite was precipitated on coating A2 surface (Fig. 12b). After 7 days' immersion in PBS, an apatite layer covered most areas and the number of plate-like HA crystals increased on the coating A1 and coating A3 surface (Fig. 12c). This suggests the formation of new apatite layer on those coating surfaces. However, the amount of apatite slightly increased on the surface of the coating A2 and only minor changes were observed its surface (Fig. 12c).

As reported from the literatures, the precipitation rate of the apatite on the HA coating is highly depended on the dissolution behavior of the coating [48]. The high dissolution rate of the coating can provide many nucleation sites, leading to a high precipitation rate [48]. The coating A2 displayed lower dissolution and precipitation rate than the coating A3, primarily due to the presence of more crystalline and lower ACP content in the coating A2. However, coating A1 with high crystallinity and phase purity also showed porous structure after PBS immersion, which attributed to the presence of nanocrystals (Fig. 4c). The nanocrystalline structure in the coating provided many nucleation sites at the areas of grain boundary for the formation of apatite crystals, promoting the precipitation of apatite [49]. This phenomenon of no plate-like crystals and smooth surface for the coatings A2 surface suggested that coating A2 with high crystallinity and *c*-axis crystalline orientation remained undissolved after immersing in PBS solution for 1 day and showed high chemical stability in PBS solution. Accordingly, the above results indicated that HA coatings with high chemical stability prevented the formation of porous surface and effectively improved the antibacterial activities.

However, it was observed that the number of *S. epidermidis* attached to the coating A2 was greater than that of *E. coli*. The less amount of *E. coli* and more *S. epidermidis* adhered on the coating A2 surface was explained by different cell morphologies of these bacteria. This observation agreed with the previous studies, indicating the larger size of *E. coli* than that of *S. epidermidis* [50]. The larger size of *E. coli* contributed to the less *E. coli* attached to the coating A2 surface in comparison with *S. epidermidis* [50,51]. The spherical morphology of the *S. epidermidis* cells might also promote their attachment ability on the smooth surface [52].

Moreover, the surface charge is also an important factor influencing bacterial adhesion. TEM results showed that the coating A2 contains columnar grains with a *c*-axis orientation (Fig. 4b). The *c*-plane of the crystalline HA was rich in phosphate and hydroxide ions and thus was a negative charge plane [51]. This negatively charged plane reduced *E. coli* adhesion due to the absence of repulsive electrostatic between the negative bacteria and the negatively charged surface [53,54]. However,

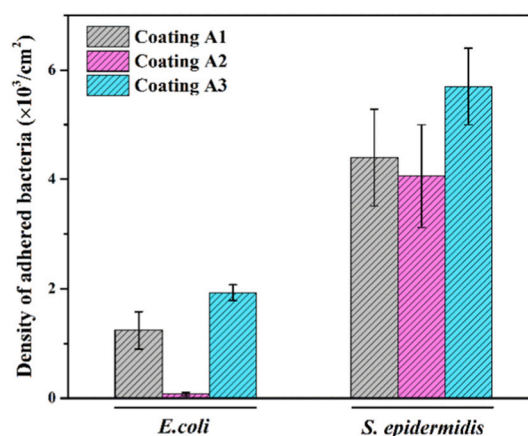


Fig. 11. Density of adhered bacteria on all coatings.

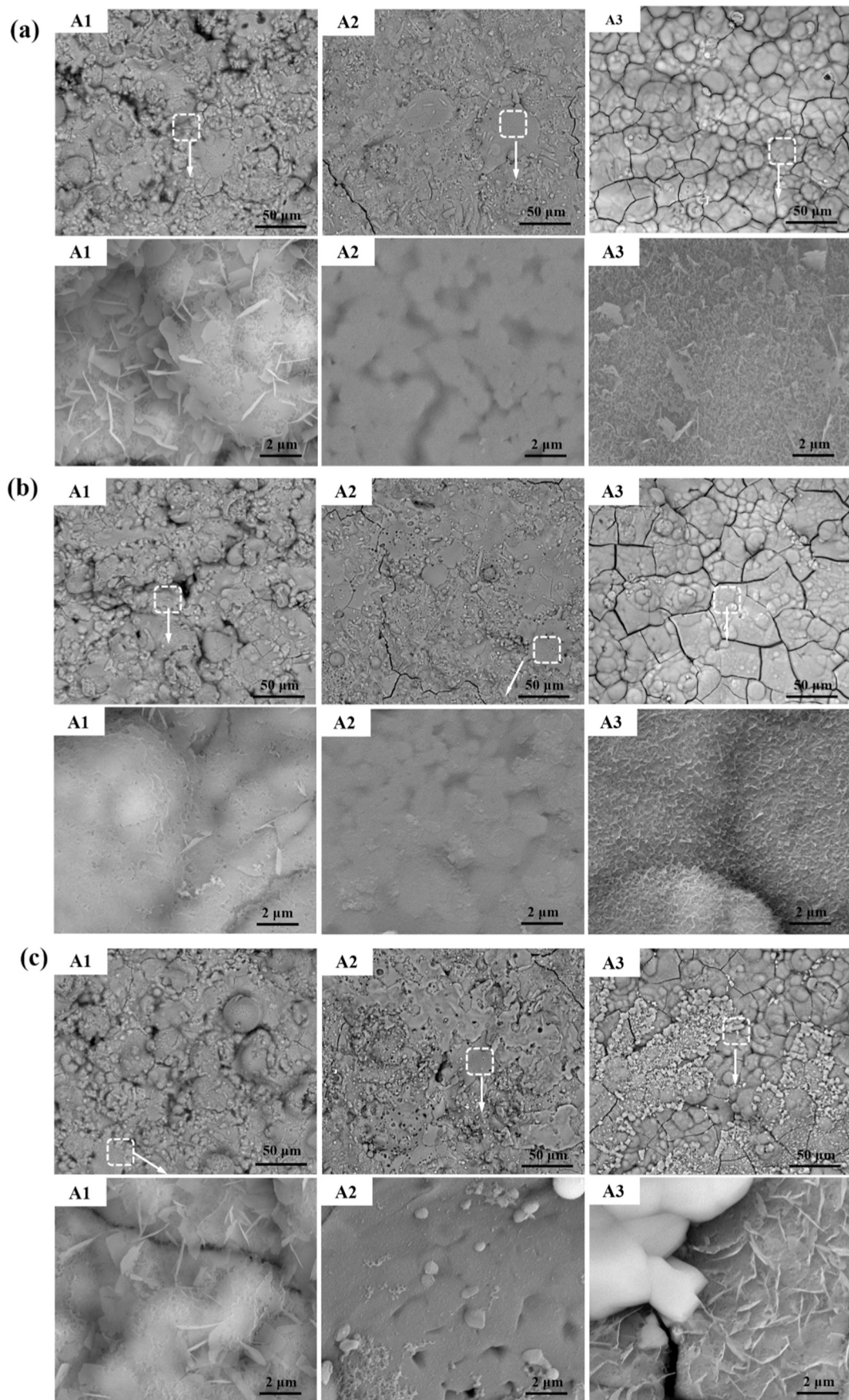


Fig. 12. Surface morphology of the coatings A1, A2 and A3 with the incubation time of (a) 1 day, (b) 5 days and (c) 7 days.

the adhesion for *S. epidermidis* on coating A2 was less affected by the exposure of *c* plane, which could be attributed to the thick and rigid peptidoglycan layer of the *S. epidermidis* [54]. Our study indicated that the HA coating with *c*-axis crystalline orientation had excellent biocompatibility and antibacterial ability. However, the mechanism of the cellular response to the *c*-axis crystalline orientation and the bacterial adhesion is still unclear.

#### 4. Conclusion

Three kinds of HA coatings with different phase structures were deposited using APS technology. The first kind of HA coating (A1) exhibited high crystallinity (>90%), the microstructure of the second of HA coating (A2) had the *c*-axis crystalline orientation characteristics and high crystallinity (> 85%), and the third kind of coating (A3) showed low crystallinity (<50%). The effects of crystallographic textures of the coatings on their biocompatibility and antibacterial ability were examined. The *in vitro* bioactivity study showed that the proliferation of osteoblasts on the HA coating with *c*-axis crystalline orientation was remarkably higher than that on the other coatings without the orientation structure. Further antibacterial testing revealed that the *c*-axis oriented coating restrained the bacterial adhesion, and the antibacterial effect was more pronounced for the Gram-negative bacteria than that of the Gram-positive bacteria. The findings suggested the outstanding chemical stability, bioactivity and antibacterial activity of the *c*-axis oriented HA coatings which gave insight into the designing and fabrication of the HA coatings structures with promoted osseointegration and stability for biomedical applications.

#### CRedit authorship contribution statement

**Xiaomei Liu:** Conceptualization, Methodology, Investigation, Experimental procedure, Formal analysis, Writing - Original Draft, Visualization.

**Dingyong He:** Conceptualization, Supervision, Writing - Review & Editing, Project administration.

**Zheng Zhou:** Conceptualization, Investigation, Formal analysis.

**Xingye Guo:** Writing - Review & Editing.

**Yi Liu:** Investigation, Methodology, Formal analysis.

**Wenjia Hou:** Methodology, Formal analysis.

**Hu Li:** Conceptualization, Supervision, Methodology, Formal analysis, Writing - Review & Editing.

#### Declaration of competing interest

The authors declare that they have no known competing financial interests or personal relationships that could have appeared to influence the work reported in this paper.

#### Acknowledgments

The authors would like to thank the funding support from the National Natural Science Foundation of China (Grant No. 51471010) and the National Natural Science Fund for Innovative Research Groups (Grant No. 51621003).

#### References

- [1] P.-I. Brånemark, U. Breine, R. Adell, B.O. Hansson, J. Lindström, Å. Ohlsson, Intraosseous anchorage of dental prostheses: I. Experimental studies, *Scand. J. Plast. Reconstr. Surg.* 3 (2) (1969) 81–100, <https://doi.org/10.3109/02844316909036699>.
- [2] C.Y. Guo, J.P. Matinlinna, A.T.H. Tang, Effects of surface charges on dental implants: past, present, and future, *Int. J. Biomater.* 12 (2012), 381535, <https://doi.org/10.1155/2012/381535>.
- [3] S.V. Dorozhkin, Calcium orthophosphate-based biocomposites and hybrid biomaterials, *J. Mater. Sci.* 44 (9) (2009) 2343–2387, <https://doi.org/10.1007/s10853-008-3124-x>.
- [4] R.B. Heimann, Plasma-sprayed hydroxyapatite-based coatings: chemical, mechanical, microstructure, and biomedical properties, *J. Therm. Spray Technol.* 25 (5) (2016) 827–850, <https://doi.org/10.1007/s11666-016-0421-9>.
- [5] Q.Z. Chen, G.A. Thouas, Metallic implant biomaterials, *Mater. Sci. Eng. R. Rep.* 87 (2015) 1–57, <https://doi.org/10.1016/j.mser.2014.10.001>.
- [6] H.W. Kim, Y.H. Koh, L.H. Li, S. Lee, H.E. Kim, Hydroxyapatite coating on titanium substrate with titania buffer layer processed by sol-gel method, *Biomaterials* 25 (13) (2004) 2533–2538, <https://doi.org/10.1016/j.biomaterials.2003.09.041>.
- [7] Y.H. Jeong, H.C. Choe, W.A. Brantley, Silicon-substituted hydroxyapatite coating with Si content on the nanotube-formed Ti-Nb-Zr alloy using electron beam-physical vapor deposition, *Thin Solid Films* 546 (2013) 189–195, <https://doi.org/10.1016/j.tsf.2013.05.130>.
- [8] V. Kosma, T. Tsoufis, T. Koliou, A. Kazantzis, K. Beltsios, J.T.M. De Hosson, D. Gourmis, Fibrous hydroxyapatite-carbon nanotube composites by chemical vapor deposition. In situ fabrication, structural and morphological characterization, *Mater. Sci. Eng. B* 178 (7) (2013) 457–464, <https://doi.org/10.1016/j.mseb.2012.11.026>.
- [9] Y.M. Wang, X.M. Liu, T.T. Fan, Z. Tan, Z. Zhou, D.Y. He, *In vitro* evaluation of hydroxyapatite coating with (002) crystallographic texture deposited by micro-plasma spraying, *Mater. Sci. Eng. C* 75 (2017) 596–601, <https://doi.org/10.1016/j.msec.2017.02.119>.
- [10] L. Zhao, K. Bobzin, F. Ernst, J. Zwick, E. Lugscheider, Study on the influence of plasma spray processes and spray parameter on the structure and crystallinity of hydroxyapatite coatings, *Materialwiss. Werkst.* 37 (6) (2006) 516–520, <https://doi.org/10.1002/mawe.200600029>.
- [11] K.A. Khor, H. Li, P. Cheang, S.Y. Boey, *In vitro* behavior of HVOF sprayed calcium phosphate splats and coatings, *Biomaterials* 24 (5) (2003) 723–735, [https://doi.org/10.1016/S0142-9612\(02\)00404-0](https://doi.org/10.1016/S0142-9612(02)00404-0).
- [12] R. Drevet, N.B. Jaber, J. Fauré, A. Tara, A. Ben Cheikh Larbi, H. Benhayoune, Electrophoretic deposition (EPD) of nano-hydroxyapatite coatings with improved mechanical properties on prosthetic Ti6Al4V substrates, *Surf. Coat. Technol.* 301 (2016) 94–99, <https://doi.org/10.1016/j.surfcoat.2015.12.058>.
- [13] Q.Y. Chen, Y.L. Zou, X. Chen, X.B. Bai, G.C. Ji, H.L. Yao, H.T. Wang, F. Wang, Morphological, structural and mechanical characterization of cold sprayed hydroxyapatite coating, *Surf. Coat. Technol.* 357 (2019) 910–923, <https://doi.org/10.1016/j.surfcoat.2018.10.056>.
- [14] S. Vahabzadeh, M. Roy, A. Bandyopadhyay, S. Bose, Phase stability and biological property evaluation of plasma sprayed hydroxyapatite coatings for orthopedic and dental applications, *Acta Biomater.* 17 (2015) 47–55, <https://doi.org/10.1016/j.actbio.2015.01.022>.
- [15] K.A. Gross, C.C. Berndt, H. Herman, Amorphous phase formation in plasma-sprayed hydroxyapatite coatings, *J. Biomed. Mater. Res.* 31 (3) (1998) 407–414, [https://doi.org/10.1002/\(SICI\)1097-4636\(19980305\)39:3<407::AID-JBM9>3.0.CO;2-N](https://doi.org/10.1002/(SICI)1097-4636(19980305)39:3<407::AID-JBM9>3.0.CO;2-N).
- [16] W.C. Xue, S.Y. Tao, X.Y. Liu, X.B. Zheng, C.X. Ding, *In vivo* evaluation of plasma sprayed hydroxyapatite coatings having different crystallinity, *Biomaterials* 25 (3) (2004) 415–421, [https://doi.org/10.1016/S0142-9612\(03\)00545-3](https://doi.org/10.1016/S0142-9612(03)00545-3).
- [17] R.B. Heimann, Thermal spraying of biomaterials, *Surf. Coat. Technol.* 201 (5) (2006) 2012–2019, <https://doi.org/10.1016/j.surfcoat.2006.04.052>.
- [18] L. Chou, B. Marek, W.R. Wagner, Effects of hydroxylapatite coating crystallinity on biocompatibility, cell attachment efficiency and proliferation *in vitro*, *Biomaterials* 20 (10) (1999) 977–985, [https://doi.org/10.1016/S0142-9612\(98\)00254-3](https://doi.org/10.1016/S0142-9612(98)00254-3).
- [19] Y.M. Wang, T.T. Fan, Z. Zhou, D.Y. He, Hydroxyapatite coating with strong (002) crystallographic texture deposited by micro-plasma spraying, *Mater. Lett.* 185 (2006) 484–487, <https://doi.org/10.1016/j.matlet.2016.09.068>.
- [20] X.M. Liu, D.Y. He, Z. Zhou, G.H. Wang, Z.J. Wang, X. Wu, Z. Tan, Atmospheric plasma-sprayed hydroxyapatite coatings with (002) texture, *J. Therm. Spray Technol.* 27 (8) (2018) 1291–1301, <https://doi.org/10.1007/s11666-018-0768-1>.
- [21] A. Peetsch, C. Greulich, D. Braun, C. Stroetges, H. Rehage, B. Siebers, M. Köller, M. Epple, Silver-doped calcium phosphate nanoparticles: synthesis, characterization and toxic effects toward mammalian and prokaryotic cells, *Colloids Surf. B* 102 (2013) 724–729, <https://doi.org/10.1016/j.colsurfb.2012.09.040>.
- [22] M. Turkoz, A.O. Atilla, Z. Evis, Silver and fluoride doped hydroxyapatites: investigation by microstructure, mechanical and antibacterial properties, *Ceram. Int.* 39 (8) (2013) 8925–8931, <https://doi.org/10.1016/j.ceramint.2013.04.088>.
- [23] T.N. Kim, Q.L. Feng, J.O. Kim, J. Wu, H. Wang, G.C. Chen, F.Z. Cui, Antimicrobial effect of metal ions (Ag<sup>+</sup>, Cu<sup>2+</sup>, Zn<sup>2+</sup>) in hydroxyapatite, *J. Mater. Sci. Mater. Med.* 9 (3) (1998) 129–134, <https://doi.org/10.1023/A:1008811501734>.
- [24] G. Singh, S. Singh, S. Prakash, Surface characterization of plasma sprayed pure and reinforced hydroxyapatite coating on Ti6Al4V alloy, *Surf. Coat. Technol.* 205 (2011) 4814–4820, <https://doi.org/10.1016/j.surfcoat.2011.04.064>.
- [25] V.F. Shamray, V.P. Sirotinkin, I.V. Smirnov, V.I. Kalita, A.Yu. Fedotov, S. M. Barinov, V.S. Komlev, Structure of the hydroxyapatite plasma-sprayed coatings deposited on pre-heated titanium substrates, *Ceram. Int.* 43 (2017) 9105–9109, <https://doi.org/10.1016/j.ceramint.2017.04.057>.
- [26] L. Fanni, B.A. Aebersold, D.T.L. Alexander, L. Ding, M. Morales Masis, S. Nicolay, C. Ballif, *c*-texture versus *a*-texture low pressure metalorganic chemical vapor deposition ZnO films: lower resistivity despite smaller grain size, *Thin Solid Films* 565 (2014) 1–6, <https://doi.org/10.1016/j.tsf.2014.06.033>.
- [27] B. Bideau, J. Bras, S. Saini, C. Daneault, E. Loranger, Mechanical and antibacterial properties of a nanocellulose-polypropylene multilayer composite, *Mater. Sci. Eng. C* 69 (2016) 977–984, <https://doi.org/10.1016/j.msec.2016.08.005>.
- [28] D.Y. Kwok, A.W. Neumann, Contact angle measurement and contact angle interpretation, *Adv. Colloid Interf. Sci.* 81 (3) (1999) 167–249, [https://doi.org/10.1016/S0001-8686\(98\)00087-6](https://doi.org/10.1016/S0001-8686(98)00087-6).

- [29] D.K. Owens, R.C. Wendt, Estimation of the surface free energy of polymers, *Appl. Polym. Sci.* 13 (8) (1969) 1741–1747, <https://doi.org/10.1002/app.1969.070130815>.
- [30] F.M. Fowkes, Attractive forces at interfaces, *Ind. Eng. Chem.* 56 (12) (1964) 40–52, <https://doi.org/10.1021/ie50660a008>.
- [31] E.A. Dos Santos, M. Farina, G.A. Soares, K. Anselme, Surface energy of hydroxyapatite and  $\beta$ -tricalcium phosphate ceramics driving serum protein adsorption and osteoblast adhesion, *Mater. Sci-Mater. M.* 19 (6) (2008) 2307–2316, <https://doi.org/10.1007/s10856-007-3347-4>.
- [32] Y. Liu, Z.H. Dang, Y.Y. Wang, J. Huang, H. Li, Hydroxyapatite/graphene-nanosheet composite coatings deposited by vacuum cold spraying for biomedical applications: inherited nanostructures and enhanced properties, *Carbon* 67 (2014) 250–259, <https://doi.org/10.1016/j.carbon.2013.09.088>.
- [33] J. Huang, Y.F. Gong, Y. Liu, X.K. Suo, H. Li, Developing titania-hydroxyapatite-reduced graphene oxide nanocomposite coatings by liquid flame spray deposition for photocatalytic applications, *J. Eur. Ceram. Soc.* 37 (12) (2017) 3705–3711, <https://doi.org/10.1016/j.jeurceramsoc.2017.02.029>.
- [34] Y.X. Liu, J. Huang, S.Y. Ding, Y. Liu, J.H. Yuan, H. Li, Deposition characterization, and enhanced adherence of *Escherichia coli* bacteria on flame-sprayed photocatalytic titania-hydroxyapatite coatings, *J. Therm. Spray Technol.* 22 (6) (2013) 1053–1062, <https://doi.org/10.1007/s11666-013-9948-1>.
- [35] X.L. Wang, B. Li, L.X. Zhou, J.W. Ma, X.L. Zhang, H.P. Li, H.P. Wang, C.Y. Liang, S. M. Liu, H.S. Wang, Influence of surface structures on biocompatibility of TiO<sub>2</sub>/HA coatings prepared by MAO, *Mater. Chem. Phys.* 215 (2018) 339–345, <https://doi.org/10.1016/j.matchemphys.2018.05.037>.
- [36] G. Zhao, Z. Schwartz, M. Wieland, F. Rupp, J. Geis-Gerstorfer, D.L. Cochran, B. D. Boyan, High surface energy enhances cell response to titanium substrate microstructure, *J. Biomed. Mater. Res. A* 74 (1) (2005) 49–58, <https://doi.org/10.1002/jbm.a.30320>.
- [37] C. Eriksson, H. Nygren, K. Ohlson, Implantation of hydrophilic and hydrophobic titanium discs in rat tibia: cellular reactions on the surfaces during the first 3 weeks in bone, *Biomaterials* 25 (19) (2004) 4759–4766, <https://doi.org/10.1016/j.biomaterials.2003.12.006>.
- [38] Q.H. Hu, Z. Tan, Y.K. Liu, J.H. Tao, Y.R. Cai, M. Zhang, H.H. Pan, X.R. Xu, R. K. Tang, Effect of crystallinity of calcium phosphate nanoparticles on adhesion, proliferation, and differentiation of bone marrow mesenchymal stem cells, *J. Mater. Chem.* 17 (44) (2007) 4690–4698, <https://doi.org/10.1039/B710936A>.
- [39] E.A. dos Santos, S. Moldovan, M. Mateescu, J. Faerber, M. Acosta, H. Pelletier, K. Anselme, J. Werckmann, Physical-chemical and biological behavior of an amorphous calcium phosphate thin film produced by RF-magnetron sputtering, *Mater. Sci. Eng. C* 32 (7) (2012) 2086–2095, <https://doi.org/10.1016/j.msec.2012.05.041>.
- [40] Z. Schwartz, C.H. Lohmann, A.K. Vocke, V.L. Sylvia, D.L. Cochran, D.D. Dean, B. D. Boyan, Osteoblast response to titanium surface roughness and 1 $\alpha$ , 25-(OH) 2D<sub>3</sub> is mediated through the mitogen-activated protein kinase (MAPK) pathway, *J. Biomed. Mater. Res.* 56 (3) (2001) 417–426, [https://doi.org/10.1002/1097-4636\(20010905\)56:3<417::AID-JBM1111>3.0.CO;2-K](https://doi.org/10.1002/1097-4636(20010905)56:3<417::AID-JBM1111>3.0.CO;2-K).
- [41] M. Okada, T. Matsumoto, Synthesis and modification of apatite nanoparticles for use in dental and medical applications, *Jpn. Dent. Sci. Rev.* 51 (4) (2015) 85–95, <https://doi.org/10.1016/j.jdsr.2015.03.004>.
- [42] M. Ohgaki, T. Kizuki, M. Katsura, K. Yamashita, Manipulation of selective cell adhesion and growth by surface charges of electrically polarized hydroxyapatite, *J. Biomed. Mater. Res.* 57 (3) (2001) 366–373, [https://doi.org/10.1002/1097-4636\(20011205\)57:3<366::AID-JBM1179>3.0.CO;2-X](https://doi.org/10.1002/1097-4636(20011205)57:3<366::AID-JBM1179>3.0.CO;2-X).
- [43] W. Chen, T. Long, Y.J. Guo, Z.A. Zhu, Y.P. Guo, Hydrothermal synthesis of hydroxyapatite coatings with oriented nanorod arrays, *RSC Adv.* 4 (1) (2014) 185–191, <https://doi.org/10.1039/C3RA43664K>.
- [44] D. Campoccia, L. Montanaro, C.R. Arciola, A review of the biomaterials technologies for infection-resistant surfaces, *Biomaterials* 34 (34) (2013) 8533–8554, <https://doi.org/10.1016/j.biomaterials.2013.07.089>.
- [45] E. Preedy, S. Perni, D. Nipič, K. Bohinc, P. Prokopovich, Surface roughness mediated adhesion forces between borosilicate glass and gram-positive bacteria, *Langmuir* 30 (31) (2014) 9466–9476, <https://doi.org/10.1021/la501711i>.
- [46] G. Harkes, J. Feijen, J. Dankert, Adhesion of *Escherichia coli* on a series of poly (methacrylates) differing in charge and hydrophobicity, *Biomaterials* 12 (9) (1991) 853–860, [https://doi.org/10.1016/0142-9612\(91\)90074-K](https://doi.org/10.1016/0142-9612(91)90074-K).
- [47] T. Nonami, H. Taoda, N.T. Hue, E. Watanabe, K. Iseda, M. Tazawa, M. Fukaya, Apatite formation on TiO<sub>2</sub> photocatalyst film in a pseudo body solution, *Mater. Res. Bull.* 33 (1) (1998) 125–131, [https://doi.org/10.1016/S0025-5408\(97\)00197-9](https://doi.org/10.1016/S0025-5408(97)00197-9).
- [48] Q.Y. Zhang, J.Y. Chen, J.M. Feng, Y. Cao, C.L. Deng, X.D. Zhang, Dissolution and mineralization behaviors of HA coatings, *Biomaterials* 24 (26) (2003) 4741–4748, [https://doi.org/10.1016/S0142-9612\(03\)00371-5](https://doi.org/10.1016/S0142-9612(03)00371-5).
- [49] B.D. Hahn, J.M. Lee, D.S. Park, J.J. Choi, J. Ryu, W.H. Yoon, J.H. Choi, B.K. Lee, H. E. Kim, S.G. Kim, Enhanced bioactivity and biocompatibility of nanostructured hydroxyapatite coating by hydrothermal annealing, *Thin Solid Films* 519 (22) (2011) 8085–8090, <https://doi.org/10.1016/j.tsf.2011.07.008>.
- [50] A. Almaguer-Flores, P. Silva-Bermudez, R. Galicia, S.E. Rodil, Bacterial adhesion on amorphous and crystalline metal oxide coatings, *Mater. Sci. Eng. C* 57 (2015) 88–99, <https://doi.org/10.1016/j.msec.2015.07.031>.
- [51] M. Abrego, P. Kingshott, S.L. McArthur, Electrospun polystyrene fiber diameter influencing bacterial attachment, proliferation, and growth, *ACS Appl. Mater. Interfaces* 7 (14) (2015) 7644–7652, <https://doi.org/10.1021/acsami.5b00453>.
- [52] N. Mitik-Dineva, J. Wang, V.K. Truong, P. Stoddart, F. Malherbe, R.J. Crawford, E. P. Ivanova, *Escherichia coli*, *Pseudomonas aeruginosa*, and *Staphylococcus aureus* attachment patterns on glass surfaces with nanoscale roughness, *Curr. Microbiol.* 58 (3) (2009) 268–273, <https://doi.org/10.1007/s00284-008-9320-8>.
- [53] A. Venault, H.S. Yang, Y.C. Chiang, B.S. Lee, R.C. Ruaan, Y. Chang, Bacterial resistance control on mineral surfaces of hydroxyapatite and human teeth via surface charge-driven antifouling coatings, *ACS Appl. Mater. Interfaces* 6 (5) (2014) 3201–3210, <https://doi.org/10.1021/am404780w>.
- [54] B. Gottenbos, D.W. Grijpma, H.C. van der Mei, J. Feijen, H.J. Busscher, Antimicrobial effects of positively charged surfaces on adhering gram-positive and gram-negative bacteria, *J. Antimicrob. Chemother.* 48 (1) (2001) 7–13, <https://doi.org/10.1093/jac/48.1>.